J. Fluid Mech. (2012), *vol.* 692, *pp.* 53–77.
doi:10.1017/jfm.2011.496

Equilibrium gas–liquid–solid contact angle from density-functional theory

Antonio Pereira and Serafim Kalliadasis†

Department of Chemical Engineering, Imperial College London, London SW7 2AZ, UK

(Received 12 March 2010; revised 12 September 2011; accepted 7 November 2011; first published online 15 December 2011)

We investigate the equilibrium of a fluid in contact with a solid boundary through a density-functional theory. Depending on the conditions, the fluid can be in one phase, gas or liquid, or two phases, while the wall induces an external field acting on the fluid particles. We first examine the case of a liquid film in contact with the wall. We construct bifurcation diagrams for the film thickness as a function of the chemical potential. At a specific value of the chemical potential, two equally stable films, a thin one and a thick one, can coexist. As saturation is approached, the thickness of the thick film tends to infinity. This allows the construction of a liquid–gas interface that forms a well-defined contact angle with the wall.

Key words: contact lines, non-continuum effects

1. Introduction

Wetting phenomena have received considerable attention over the past few decades – comprehensive and detailed reviews are given by de Gennes (1985), Schick (1990), Indekeu (1994) and Bonn *et al.* (2009). Central to any description of wetting is the presence of a contact line, which involves a three-phase conjunction (gas–liquid–solid). In the case of dynamic wetting, the associated moving contact line problem is characterized by a stress singularity at the contact line. As a consequence, formulating this problem in the framework of conventional fluid mechanics leads to fundamental difficulties concerning the modelling of the contact line region (Moffat 1963; Huh & Scriven 1971; Dussan & Davis 1974). Accordingly, a variety of models have been proposed to alleviate these difficulties and to address the behaviour of the associated dynamic contact angle, with the most popular approaches being the replacement of the no-slip condition with a slip model or the elimination of the contact line altogether with the use of a thin precursor layer. More recently, new approaches/theories have appeared, based, for example, on local diffuse-interface/Cahn–Hilliard type approaches, which, in general, cannot be rigorously justified. Other recent approaches include hybrid molecular-hydrodynamic simulations. However, the questions of how to coarse-grain rigorously from the micro- to the macro-scale and how to transfer molecular information accurately to the macro-scale have not been adequately addressed as yet.

The difficulties with the contact line region stem from the multi-scale nature of the problem. At the macroscale, the usual laws of hydrodynamics apply. At the nanoscale, intermolecular interactions, often described by molecular dynamics/Monte

† Email address for correspondence: s.kalliadasis@imperial.ac.uk

Carlo simulations, dominate. Yet, phenomena occurring at the nanoscale often manifest themselves at the macroscale (where individual molecules are not considered, or equivalently the hydrodynamic laws consider a very large number of molecules at the same time). Despite drastic improvements in computational power, molecular simulations are still only applicable for small fluid volumes.

A compromise between conventional hydrodynamics and molecular simulations can be achieved by density-functional theory (DFT). On the one hand, DFT is able to retain the microscopic details of a macroscopic system at a computational cost significantly lower than that used in molecular simulations. On the other hand, DFT is rigorous compared to conventional phenomenological approaches. It is applicable for both uniform and non-uniform (density exhibits spatial variation) as well as confined systems (e.g. in the presence of a wall) within a self-consistent theoretical framework provided by the statistical mechanics of fluids. At the same time, substantial progress has been made in recent years in the development of realistic free-energy functionals that take into account the thermodynamic non-ideality attributed to the various intermolecular forces. The papers by Evans (1979), Tarazona (1985) and Argaman & Makov (2000) outline a DFT framework currently widely accepted by the 'statistical mechanics of fluids' community and which has also been used successfully in describing equilibrium configurations in many different contexts, from fluids in pores to liquid crystals, polymers and molecular self-assembly.

Several studies have examined the equilibrium of liquids in contact with solids in different settings and in the framework of DFT/statistical mechanics of fluids. For example, Pismen (2002) adopted a DFT approach based on a free-energy functional proposed by Landau & Lifshitz (1980). This study focused primarily on a one-dimensional (1D) configuration, namely a liquid film in contact with a planar solid substrate, but it did discuss contact lines; for example, it gave an approximate expression for the equilibrium contact angle obtained from the sharp-interface limit of the DFT approach adopted and for large distances from the solid substrate. Differences between local and non-local theories in the context of the contact line were examined by Getta & Dietrich (1998) and Bauer & Dietrich (1999) using a simplified DFT approach based on a sharp-interface approximation in the direction normal to the substrate. (This approximation was scrutinized in the recent studies by Nold, Malijevský & Kalliadasis (2011*a*,*b*).) Recently, Berim & Ruckenstein (2008*a*,*b*, 2009) adopted a DFT approach based on the framework described by Evans (1979), Tarazona (1985) and Argaman & Makov (2000) to calculate nanodrops on chemically/physically inhomogeneous inclined/planar substrates and to obtain the dependence of the contact angle of nanodrops on planar horizontal substrates on the parameters of the intermolecular interactions.

Our aim here is to provide a rigorous methodology for the treatment of contact lines and in particular to construct the density profiles in the immediate vicinity of a contact line region. Our approach is also based on the DFT framework described by Evans (1979), Tarazona (1985) and Argaman & Makov (2000). We focus on the equilibrium of a fluid in contact with a planar solid substrate, whose understanding is essential for the substantially more involved dynamics. We first examine in detail the 1D case of a liquid film in contact with the substrate. Particular emphasis is given to the bifurcation diagrams for the film thickness as a function of the chemical potential. The approach of investigating wetting phenomena in terms of the film thickness was introduced a long time ago by Frumkin and Derjaguin by using the concept of disjoining pressure – see Henderson (2005) for a detailed analysis of this approach and its connection with wetting phenomena as described by DFT.

Although detailed analysis of the 1D problem, in particular density profiles, has been performed since then, especially by Evans and co-workers from the 1980s and later (e.g. Tarazona & Evans 1983; Tarazona, da Gama & Evans 1983; Evans & Parry 1990; Evans 1992), we briefly review it in the first part of our study (where we also construct by continuation bifurcation diagrams for the film thickness), as it is a necessary step prior to understanding the more involved two-dimensional (2D) case, i.e. the three-phase contact line, which is the main subject here.

As we shall demonstrate, before the construction of a three-phase contact line can be carried out, a detailed analysis of the prewetting transition is required; this transition occurs at a specific value of the chemical potential where two equally stable films, a thin one and a thick one, coexist. Through full 2D DFT computations, we show that the two thicknesses are connected through a ridge-like interface, and we observe that the extension of the transition zone between the two film thicknesses is larger in the case of a long-range potential (about 50 molecular diameters) than in the case of a short-range potential (about 10 molecular diameters, to be compared to the liquid–gas interface, which is typically a few molecular diameters thick). When the coexistence value of the chemical potential equals its saturation value, the thickness of the thick film tends to infinity. This is the case for a liquid wedge in contact with the solid substrate and with a well-defined three-phase contact line a few molecular diameters from the substrate. The wedge seems to persist for all distances from the substrate.

Hence, even though DFT is a microscopic approach, it allows for the construction of a macroscopic quantity such as contact angle. Moreover, unlike macroscopic approaches, e.g. Young's equation, which naturally require information on macroscopic parameters, such as the surface tensions between the different phases, DFT relies only on first principles, namely information related to intermolecular parameters. It also elucidates the structure of the three-phase contact line region and the precise role of fluid–fluid and fluid–solid (long- and short-range) interactions there.

2. Problem definition

2.1. *Setting*

We consider part of a simple fluid inside a domain $\mathscr{D}$ in contact with a horizontal planar substrate as shown in figure 1. The domain has a volume $\mathscr{V}$ and the interface between the domain and the substrate has an area $\mathscr{A}$. Practically, the domain size will be large, i.e. macroscopic. The system, whose boundary is denoted with the closed dashed line in the figure, is open, i.e. fluid particles can come in and out, and its surroundings are at temperature T and chemical potential μ. Depending on the conditions, the fluid can be in one phase (gas or liquid) or two phases. The fluid particles interact through a pair potential $\phi(r_{12})$, where r_{12} is the distance between the centres of mass of the particles. The main effect of the substrate is to induce a potential field $V(\boldsymbol{r})$ acting on the fluid particles, with $\boldsymbol{r}$ the position vector of the inertial centre of fluid particles. For the sake of simplicity, gravity is neglected. A Cartesian coordinate system (x, y, z) is chosen such that x and y are parallel to the wall surface while z is the outward-pointing coordinate normal to the wall. Of particular interest is the region around the solid–fluid interface.

2.2. *Density-functional theory of fluids*

An important quantity characterizing the equilibrium state of the system is the fluid density $n_0(\boldsymbol{r})$, in units of number of particles per unit volume (number density),

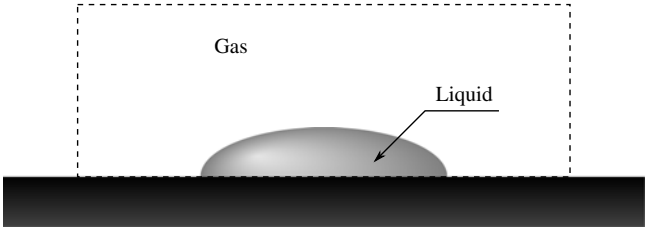

FIGURE 1. Sketch of the physical setting.

defined as (Evans 1979)

$$n_0(\boldsymbol{r}) = \left\langle \sum_{i=1}^{\bar{N}} \delta(\boldsymbol{r} - \boldsymbol{r}_i) \right\rangle, \tag{2.1}$$

where $\boldsymbol{r} \in \mathscr{D}$, $\boldsymbol{r}_i$ is the position of each individual particle and $\bar{N}$ is the total number of particles, while the symbol $\langle \ldots \rangle$ refers to the ensemble average in the grand canonical formalism, appropriate for an open system as is the case here. To obtain $n_0(\boldsymbol{r})$, we use elements from equilibrium statistical mechanics of fluids, in particular DFT. It has been shown that there exists a functional $\Omega[n]$, defined on a set of functions $n(\boldsymbol{r})$ compatible with the external potential $V_{ext}(\boldsymbol{r})$, which has the property to be at a global minimum (for a given temperature, domain, chemical potential and external potential $V_{ext}(\boldsymbol{r})$) when $n(\boldsymbol{r})$ is equal to the equilibrium density profile $n_0(\boldsymbol{r})$ (Evans 1979; Plischke & Bergersen 2006) (minimum principle). A second functional $F[n]$ can also be introduced such that $\Omega[n]$ reads

$$\Omega[n] = F[n] + \int \mathrm{d}\boldsymbol{r}\, n(\boldsymbol{r})(V_{ext}(\boldsymbol{r}) - \mu), \tag{2.2}$$

where the integral is understood to be a volume one over $\mathscr{D}$. The intrinsic free energy and the grand potential of the system at equilibrium are then equal to $F[n_0]$ and $\Omega[n_0]$, respectively (such quantities can only be defined at equilibrium).

By using variational calculus, it can be easily shown that a necessary condition for a minimum of $\Omega[n]$ is

$$\frac{\delta F[n]}{\delta n(\boldsymbol{r})} + V_{ext}(\boldsymbol{r}) = \mu. \tag{2.3}$$

This equation is supplemented by appropriate boundary conditions, i.e. the value of n outside $\mathscr{D}$. In our case, the external potential $V_{ext}(\boldsymbol{r})$ is the sum of the potential $V(\boldsymbol{r})$ due to the substrate and the interaction between the fluid molecules inside $\mathscr{D}$ and those located outside $\mathscr{D}$, whose density is specified in the boundary conditions. Note that, since our system is open (grand canonical ensemble formalism), the average number of particles, N, is not given, but it is obtained instead once $n_0(\boldsymbol{r})$ is known: $N = \int \mathrm{d}\boldsymbol{r}\, n_0(\boldsymbol{r})$. For simplicity, we drop the subscript 0 from n hereinafter.

An approximate expression for $F[n]$ can be obtained from statistical physics (Evans 1979; Sullivan 1981). Details of the equations used in the present study are given in appendix A along with the definitions and calculations of some properties of the fluid derived from them and which will be used in the next sections (for example, n_{liq} and n_{gas}). For additional details, the interested reader should consult the literature on the statistical mechanics of liquids. A good starting point is the comprehensive review by Evans (1979).

2.3. *Wall potentials*

Three types of wall potential are considered in this study. All are attractive at large distances. The first two have the same infinite repulsive part but they differ in the range of the attraction term. The short-range potential reads

$$V_{SR}(z) = \begin{cases} +\infty & \text{if } z < z_w, \\ -\epsilon_w \exp\left(-\dfrac{z - z_w}{\sigma_w}\right) & \text{if } z > z_w; \end{cases} \tag{2.4a}$$

while for the long-range one we use

$$V_{LR}(z) = \begin{cases} +\infty & \text{if } z < z_w, \\ -2\epsilon_w \left(\dfrac{1}{1 + (z - z_w)/\sigma_w}\right)^3 & \text{if } z > z_w. \end{cases} \tag{2.4b}$$

In these expressions, ϵ_w, σ_w and z_w are three wall parameters. The first two are strictly positive and are related to the strength and range of the potentials. The expressions in (2.4*a*) and (2.4*b*) are useful in that they allow us to examine the effect of the wall attraction, and in particular its range, on the fluid equilibrium state. The last wall potential has a smooth repulsive part compared to the previous ones (i.e. it is non-impulsive):

$$V_{LJ}(z) = \begin{cases} +\infty & \text{if } z < z_w, \\ 2\epsilon_w \left[\dfrac{2}{15}\left(\dfrac{\sigma_w}{z - z_w}\right)^9 - \left(\dfrac{\sigma_w}{z - z_w}\right)^3\right] & \text{if } z > z_w. \end{cases} \tag{2.4c}$$

It can be derived by considering that the wall is made of a uniform density of particles interacting with the fluid particles through a Lennard-Jones potential (see appendix B). By setting $\sigma_{w,LR} = z_{w,LR} - z_{w,LJ}$ and $\epsilon_{w,LR} = (\sigma_{w,LJ}/\sigma_{w,LR})^3\, \epsilon_{w,LJ}$, the two last potentials have the same attractive part. Finally, it is also possible to have a purely repulsive wall with no attraction (a hard or dry wall):

$$V(z) = \begin{cases} +\infty & \text{if } z < z_w, \\ 0 & \text{if } z > z_w. \end{cases} \tag{2.5}$$

3. 1D problem

3.1. *Equations*

In this section we assume that the system is invariant along the x and y directions, i.e. the density profiles depend only on z. Equation (A 4) for z such that $\boldsymbol{r} \in \mathscr{D}$ then becomes

$$\mu_r(n(z)) + \int_{-\infty}^{+\infty} \mathrm{d}z'\, n(z') \Phi_{1d}(z' - z) + V(z) = \mu, \tag{3.1a}$$

where

$$\Phi_{1d}(Z) = \iint_{-\infty}^{+\infty} \mathrm{d}x\, \mathrm{d}y\, \phi_p\left(\sqrt{x^2 + y^2 + Z^2}\right), \quad Z \equiv z' - z, \tag{3.1b}$$

and the value of n outside $\mathscr{D}$ is fixed. (In (3.1*a*) μ_r is the chemical potential of the reference system, and in (3.1*b*) ϕ_p is the perturbation part of the interaction potential; see appendix A.)

The integral in (3.1*b*) can be performed analytically (see appendix B). To solve the integral equation (3.1) numerically, a simple iterative procedure can be employed based on a Picard scheme. The integral is first computed with the values of the density obtained from the previous iteration by using a simple trapezoidal rule and then the remaining terms are solved for n, which gives the new value for the density. We found that, with the exception of unstable solutions, this scheme is robust and allows the use of an initial guess that can be far from the solution. However, convergence tends to be slow after the first iterations. This can be greatly improved by using instead a more involved scheme based on a Newton procedure in which the Jacobian matrix is appropriately simplified. Details are given in appendix C.

3.2. *Isotherms*

When the wall potential is attractive, density profiles obtained by solving (3.1) for $T < T_c$ and $\mu < \mu_{sat}(T)$, where T_c is the fluid critical temperature and $\mu_{sat}(T)$ is the saturation value of the chemical potential (see appendix A; note that, in that case, the bulk gas is the more stable phase in the absence of the wall), exhibit a bump near the wall, while far from it, it tends to the density of the gas, n_{gas} (Tarazona & Evans 1983). If μ is close enough to $\mu_{sat}(T)$, this bump is more pronounced and the fluid density in that area is roughly equal to the metastable liquid bulk density, meaning that a thin liquid film is effectively formed between the wall and the gas.

Of particular interest is the dependence of the film thickness with respect to μ for a given T. This is crucial to understanding more involved configurations such as the contact angle case examined later. Because of the spatial variation of the density, it is in fact more relevant to consider an integral norm of the density, the adsorption, which represents an excess number of particles per unit area with respect to some (uniform) bulk densities and is defined for a 1D infinite system as

$$\Gamma = \int_{-\infty}^{z_I} \mathrm{d}z\,(n(z) - n_{-\infty}) + \int_{z_I}^{+\infty} \mathrm{d}z\,(n(z) - n_{+\infty}), \tag{3.2}$$

where z_I is the position of the dividing wall–fluid interface, and $n_{-\infty}$ and $n_{+\infty}$ are the bulk quantities, which are equal in the present case to 0 and n_{gas}, respectively. The bifurcation diagrams for the isotherms are constructed with a continuation procedure that also involves an extra equation/geometric constraint that links the continuation parameter μ and n with the continuation step. Besides easily obtaining the density profiles for a wide range of values of μ, this approach has the additional benefit that it allows the computation of unstable branches, which would have been more difficult if not impossible to obtain otherwise.

Typical isotherms for the wall potential V_{LJ} in (2.4*c*) are depicted in figure 2. For very attractive walls (for example, the case $\beta_c\epsilon_w = 3$ in figure 2) and $\mu < \mu_{sat}$, the adsorption Γ is a monotonically increasing function of μ; in particular, only one solution exists for a given value of μ. At the saturation value μ_{sat}, the bulk liquid phase becomes as stable as the bulk gas one and the adsorption goes to infinity. For less attractive walls, a multi-valued S-shaped loop in the isotherm appears for values of μ, say, in $[\mu_-, \mu_+]$ and with three branches of solutions, from which the middle one is always unstable (corresponding to variational maxima for Ω). This loop is associated with the presence of a first-order phase transition with respect to the adsorption: for a certain value of $\mu \in [\mu_-, \mu_+]$, three solutions coexist, of which those in the lower and upper branches are equally stable (variational minima of Ω of equal 'depth'), and consequently the system can adopt for that value of μ two

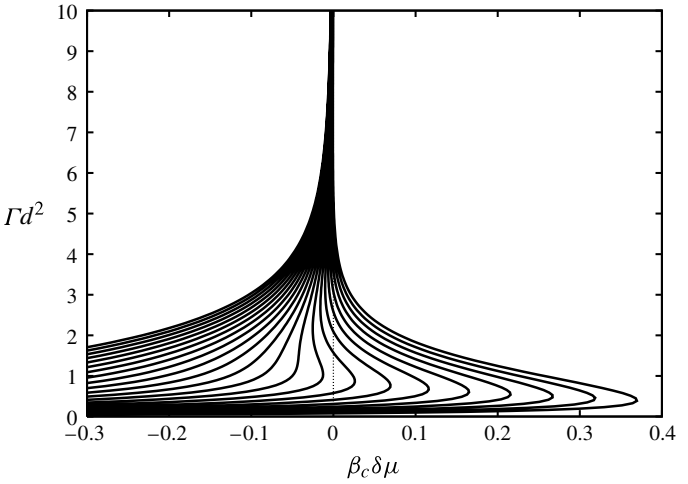

FIGURE 2. Bifurcation diagram for Γ as a function of $\delta\mu \equiv \mu - \mu_{sat}$, for the attractive wall with potential V_{LJ} (2.4*c*), $z_w = 0$ and $\sigma_w = 1.25\,d$, where d is the hard-sphere diameter (see appendix A). The temperature is $T = 0.7\,T_c$ and the dividing interface is located at $z_I = z_w$. The wall parameter $\beta_c\epsilon_w$, where $\beta_c \equiv 1/(k_B T_c)$ and k_B is the Boltzmann constant, varies from 3.0 (left curve) to 0.8 (right curve) in steps of 0.1.

different adsorptions or equivalently film thicknesses. This transition is often referred to as the 'prewetting transition' and a Maxwell construction in the variables (μ, N) can be carried out to find the coexistence value $\mu_{coex}(T)$ of the chemical potential at which the two states have the same stability. For $\mu \in [\mu_-, \mu_{coex}]$, the lower branch is stable and the upper one is metastable (Ω has two variational minima but the one in the lower branch is 'deeper'), while for $\mu \in [\mu_{coex}, \mu_+]$ the upper branch is stable and the lower one is metastable.

The value μ_{sat} imposes an upper bound on μ_{coex} as depicted in figure 5 in the case of the wall potential V_{SR} (solid line). The intersection of the μ_{coex} curve with the x axis (i.e. the $\mu = \mu_{sat}$ axis) separates this axis into two regions. On the left of the intersection point, which corresponds to the case of slightly attractive substrates (for example, $\beta_c\epsilon_w = 1.2$ in figure 3), among the three equilibrium films at $\mu = \mu_{sat}$ (including the solution $\Gamma = +\infty$), the film with the smaller adsorption is the most stable one. This is the signature of a partial wetting situation. On the right of the intersection point (for example, $\beta_c\epsilon_w = 2.2$ in figure 3), it is the film with infinite adsorption that is the most stable, and this case corresponds to the complete wetting situation.

The influence of the wall potential form on the isotherms can be assessed from figures 3 and 4, where the isotherms for the wall potentials V_{SR} and V_{LR} in (2.4*a*) and (2.4*b*), respectively, are shown. The isotherms appear qualitatively similar to those in figure 2. The effect of the potential ranges, however, becomes apparent in the upper half of the figures as, for a given isotherm, μ tends to μ_{sat} as Γd^2 goes to $+\infty$ much faster in the case of potential V_{SR} than in the case of potential V_{LR}. It is also worthwhile to note the important differences in the bottom half of the figures even though the distance from the wall is small there (i.e. the potential range is less critical): the values of μ_-, μ_{coex} and μ_+ in the two cases differ significantly. This is confirmed in figure 5, where their dependence on the strength ϵ_w of the wall potentials is depicted. The intersection of μ_{coex} with the x axis (i.e. the $\mu = \mu_{sat}$ axis)

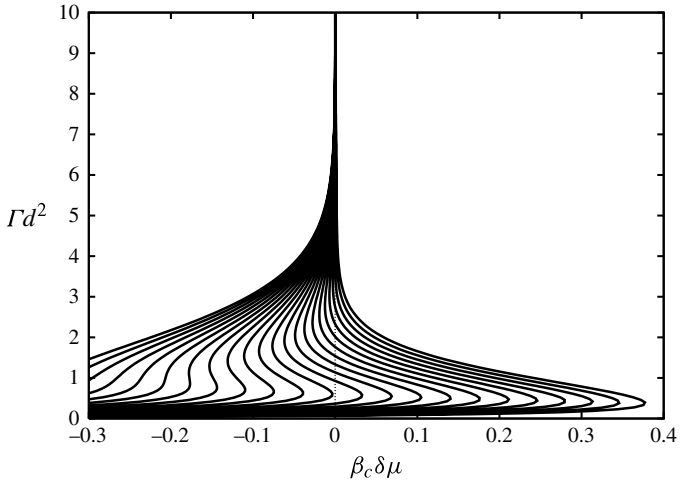

FIGURE 3. Bifurcation diagram for Γ as a function of $\delta\mu \equiv \mu - \mu_{sat}$, for the attractive wall with potential V_{SR} (2.4*a*), $z_w = 0$ and $\sigma_w = 1.25\,d$. The temperature is $T = 0.7\,T_c$ and the dividing interface is located at $z_I = z_w$. The wall parameter $\beta_c\epsilon_w$ varies from 3.4 (left curve) to 1.2 (right curve) in steps of 0.1.

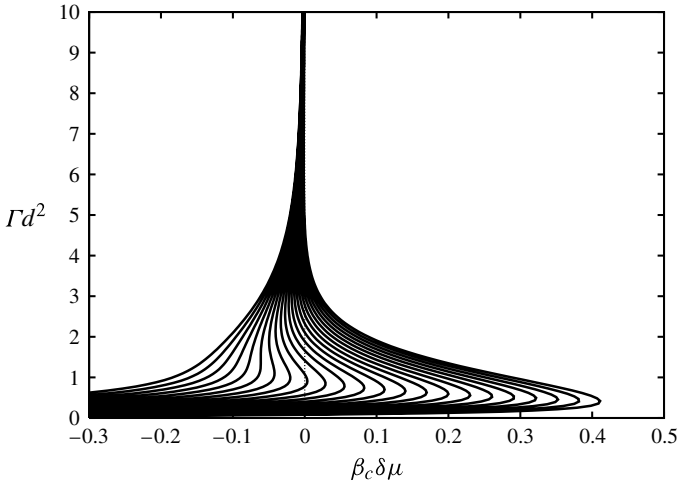

FIGURE 4. Bifurcation diagram for Γ as a function of $\delta\mu \equiv \mu - \mu_{sat}$, for the attractive wall with potential V_{LR} (2.4*b*), $z_w = 0$ and $\sigma_w = 1.25\,d$. The temperature is $T = 0.7\,T_c$ and the dividing interface is located at $z_I = z_w$. The wall parameter $\beta_c\epsilon_w$ varies from 3.4 (left curve) to 1.2 (right curve) in steps of 0.1.

in figure 5 corresponds to the partial–complete wetting transition with respect to ϵ_w. For weakly attractive walls (ϵ_w small), the wetting is partial and becomes complete for very attractive walls (ϵ_w large). In the present case, the transition occurs sooner for the short-range potential.

Finally, in appendix D we discuss a square-gradient approximation to the above DFT approach and contrast the two.

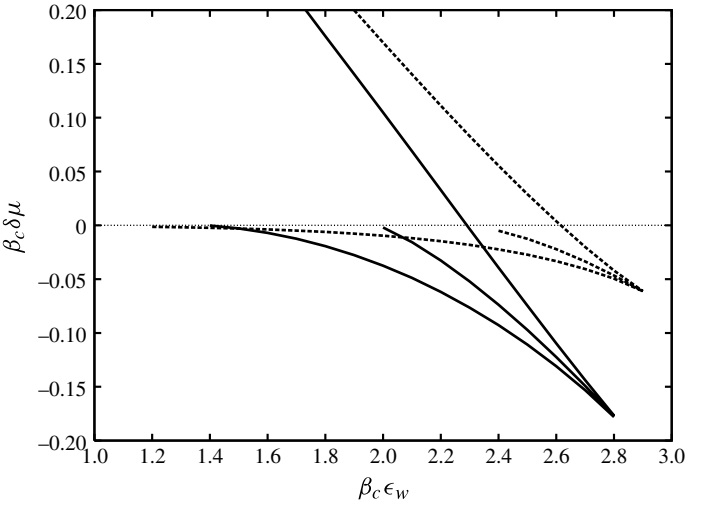

FIGURE 5. Spinodal and coexistence values (μ_-, μ_{coex} and μ_+) of the chemical potential as a function of ϵ_w. The solid lines correspond to wall potential V_{SR} and the dotted lines to wall potential V_{LR}. The remaining parameters are the same as in figures 3 and 4.

3.3. *Disjoining pressure*

The isotherms showing the adsorption as a function of the chemical potential can be related to the so-called disjoining pressure introduced by Frumkin and Derjaguin in the context of the adsorption of films in porous media (Henderson 2005). Let us denote by μ_{N_e} the conjugate parameter to N_e, the excess number of particles, and by $\mu_{N_e,0}$ the value taken by μ_{N_e} in the system surroundings. Usually, $N_b \equiv N - N_e$ is kept constant. If we now introduce

$$\Delta\mu = \mu_{N_e} - \mu_{N_e,0}, \tag{3.3}$$

the disjoining pressure is equal to (Henderson 2005)

$$\Pi = -\Delta\mu(n_{liq}(\mu_{sat}) - n_{gas}(\mu_{sat})). \tag{3.4}$$

For a 1D infinite system, one can define from Γ a film thickness l as

$$l = \Gamma/(n_{liq}(\mu_{sat}) - n_{gas}(\mu_{sat})), \tag{3.5}$$

so that the grand potential (or the disjoining pressure) can be viewed as a function of l instead of Γ. Note, however, that the value of the grand potential at l as defined above is *a priori* different from the value of the grand potential corresponding to a sharp-interface profile of thickness l as used in some approaches. From a macroscopic point of view, the disjoining pressure can be regarded as a force per unit area acting on the film surface. A positive disjoining pressure means in general that the film adsorption (or thickness) tends to increase, while, when the disjoining pressure is zero, we are at equilibrium.

For the cases considered in this study, μ_{N_e} is equal to μ. For example, let us assume that $\mathcal{V}$ is large and that the free energy can be divided into two contributions, a bulk one and a surface one, i.e. $\tilde{F}(N) = \tilde{F}_b(N_b) + \tilde{F}_e(N_e)$, where $\tilde{F}[n] = F[n] + \int \mathrm{d}\boldsymbol{r}\, n(\boldsymbol{r})V_{ext}(\boldsymbol{r})$. Then $\partial\tilde{F}_b/\partial N_b = \mu$ and, as $\mu_{N_e} = \partial\tilde{F}_e/\partial N_e$, we obtain $\mu_{N_e} = \mu$. This means that the isotherms computed previously also correspond to plots of the adsorption with respect to μ_{N_e}.

4. 2D problem

4.1. *Equations*

We now consider cases for which the translational invariance along one of the directions parallel to the substrate is broken, so that (A 4) now reads

$$\mu_r[n](x,z) + \iint_{-\infty}^{+\infty} \mathrm{d}x'\,\mathrm{d}z'\, n(x',z')\Phi_{2d}\left(\sqrt{(x'-x)^2+(z'-z)^2}\right) + V(x,z) = \mu, \tag{4.1a}$$

where (x, z) is such that $\boldsymbol{r} \in \mathscr{D}$ and

$$\Phi_{2d}(R) = \int_{-\infty}^{+\infty} \mathrm{d}y\, \phi_p\left(\sqrt{R^2+y^2}\right) \tag{4.1b}$$

with

$$R \equiv \sqrt{(x'-x)^2+(z'-z)^2}. \tag{4.1c}$$

The value of n outside $\mathscr{D}$ is fixed. The x dependence of the wall potential V could correspond, for example, to a chemically and/or topographically heterogeneous substrate.

The integral in (4.1*b*) can be performed analytically (see appendix B). The computations now are substantially more demanding compared to the previous ones, because, besides being 2D, they also usually require a much larger number of iterations to achieve convergence. As in the 1D case, we utilize a Newton scheme with an appropriately simplified Jacobian. Details are given in appendix C.

4.2. *Prewetting transition*

As demonstrated in § 3.2, for a range of values of temperature and chemical potential, there exists a first-order phase transition with respect to the adsorption Γ, also known as the prewetting transition. The interface profile in the area joining two equilibrium film thicknesses at the prewetting transition is pictured in figure 6 for the long-range wall potential in (2.4*c*). The shape of the interface between the two films appears to be sufficiently smooth compared to the density profile of a liquid–gas interface, as the interface between the films is several tens of molecular diameters long, while in the latter case it is typically only of a few molecular diameters long.

The shape of the transition area depends on the difference of the two coexisting equilibrium thicknesses and also on the range of the wall potential. In figure 7, we present the profile obtained when the wall potential is a short-range one given in (2.4*a*). The transition now between the two film thicknesses appears to be more abrupt, with a steep rim as the smaller thickness is approached, giving the profile a pancake-type shape.

4.3. *Contact angle*

We now turn to the study of the density profile when $\mu = \mu_{sat}$ and the wall is attractive with a potential given by (2.4*c*). Again, as in § 4.2, two different conditions are imposed on each side of the domain. The wall parameter ϵ_w is chosen so that a stable film of finite thickness can be sustained on the wall. According to figure 2, this is true for V_{LJ} when $\beta_c\epsilon_w$ is at least in the range 0.8–1.4. The corresponding 1D density profile computed in § 3 will make up the boundary condition on the left side of the domain. On the right side, a thick film of arbitrary thickness h_{right} and shape

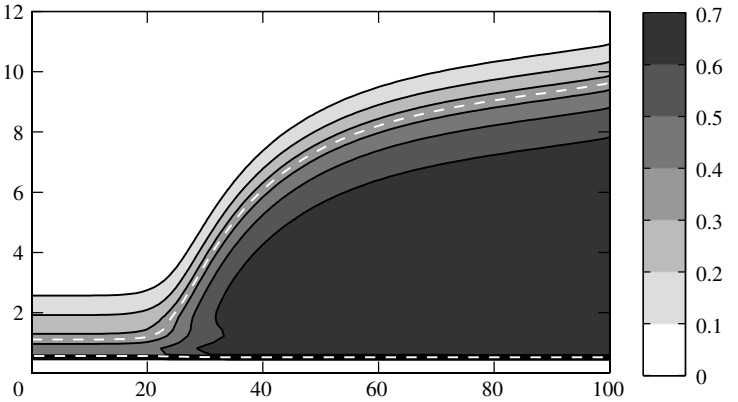

FIGURE 6. Equilibrium density profile between two equilibrium film thicknesses for the long-range wall potential V_{LJ} given by (2.4*c*). The temperature is $T = 0.7\,T_c$ and the chemical potential is $\mu = \mu_{coex}$. The wall parameters are $\beta_c\epsilon_w = 1.5$, $\sigma_w = 1.25\,d$ and $z_w = 0$. The greyscale values provided to the right of the figure correspond to the level values of nd^3. The white dashed line is the contour of $(n_{liq} + n_{gas})d^3/2$.

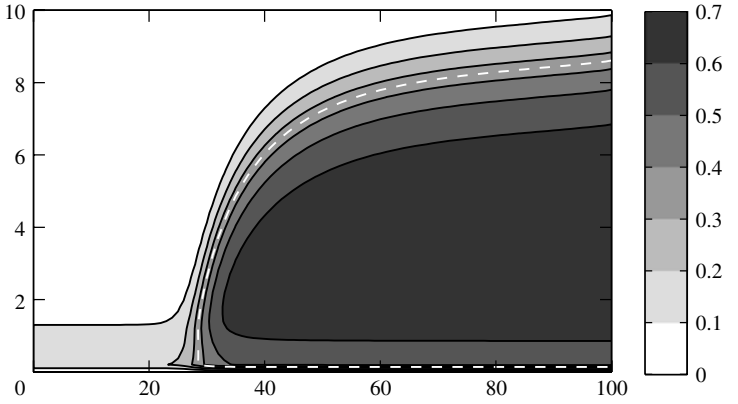

FIGURE 7. Equilibrium density profile between two equilibrium film thicknesses for the short-range wall potential V_{SR} given by (2.4*a*). The temperature is $T = 0.7\,T_c$ and the chemical potential is $\mu = \mu_{coex}$. The wall parameters are $\beta_c\epsilon_w = 2.0$, $\sigma_w = 1.25\,d$ and $z_w = 0$. The greyscale values provided to the right of the figure correspond to the level values of nd^3. The white dashed line is the contour of $(n_{liq} + n_{gas})d^3/2$.

is imposed (unlike the equilibrium film to the left, to the right we do not have an equilibrium film). For simplicity, the latter is taken to be

$$n_{right}(z) = \begin{cases} 0 & \text{if } z < z_w, \\ n_{liq} & \text{if } z_w < z < z_w + h_{right}, \\ n_{gas} & \text{if } z > z_w + h_{right}. \end{cases} \tag{4.2}$$

An equilibrium density profile for an attractive wall obtained under these conditions is depicted in figure 8. The main feature is the presence of a well-formed angle between the two phases. This is more evident in the current profiles than in the profiles obtained in § 4.2, quite likely because now the film profile on the right side

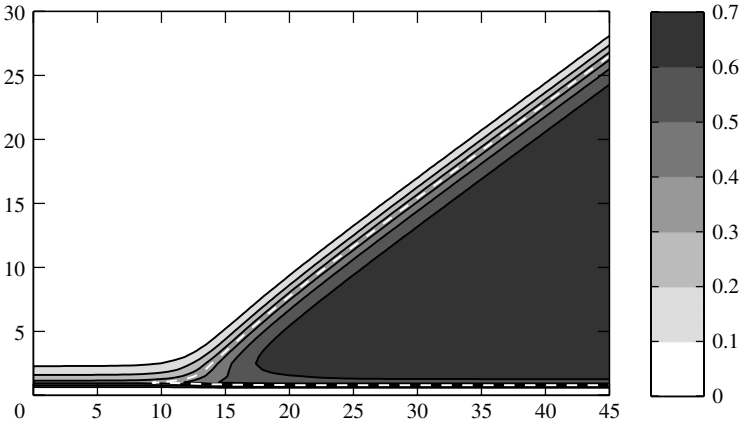

FIGURE 8. Equilibrium density profile for a fluid in contact with an attractive wall, whose potential is V_{LJ} (2.4*c*). The temperature is $T = 0.7\,T_c$, and the chemical potential is $\mu = \mu_{sat}$. The wall parameters are $\beta_c \epsilon_w = 1.3$, $\sigma_w = 1.25\,d$ and $z_w = 0$. The contact angle is close to 37°. The white dashed line is the contour of $(n_{liq} + n_{gas})d^3/2$.

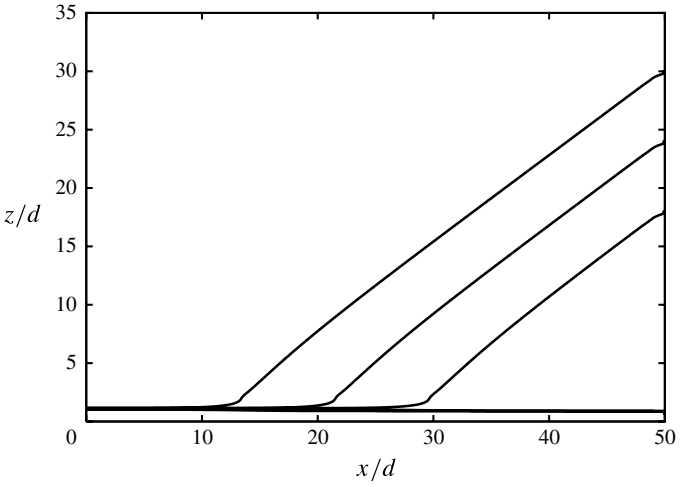

FIGURE 9. Density level curves corresponding to $(n_{liq} + n_{gas})d^3/2$ for three different values of film thickness h_{right} imposed on the right side of the domain: $h_{right}/d = 30$ (left curve), 24 and 18 (right curve). In all cases, the same film is imposed on the left side of the domain. All parameters are identical to those of figure 8.

of the domain is no longer an equilibrium one. Note also the liquid film present in front of the contact line area, as the wall is attractive. Moreover, it is important to establish that the profile is not affected by the film thickness to the right. Indeed, as demonstrated in figure 9, the thickness of the film in the right side of the domain has little influence on the density profile, since, for all values of h_{right}, the level curves are parallel to each other sufficiently far from the contact line.

A cut in the density profile displayed in figure 8 far from the contact area and normal to the liquid–gas interface is shown in figure 10. A comparison with the profile of a liquid–gas interface with no wall present reveals that the two are very close to each other: away from the contact line, the interface shape is thus not affected by the

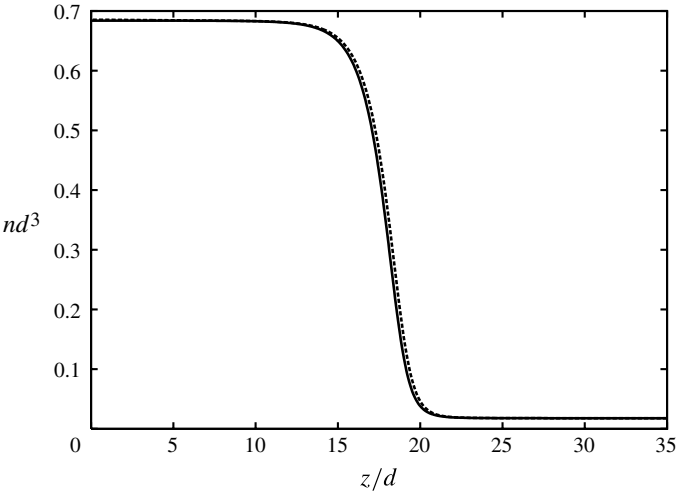

FIGURE 10. Liquid–gas interface in the absence of the wall (solid line) and cut in the density profile pictured in figure 8 normal to the liquid–gas interface (dotted line). The two profiles are very close to each other.

wall, and it is like having the usual liquid–gas interface there. However, a deviation from the liquid–gas interface occurs in the three-phase area, where a small incurvation of the density profile towards the wall is observed. We shall return to this point shortly.

The surface tension of an interface between two bulk phases can be related to the grand potential Ω of the infinite system via

$$\sigma = \frac{\Omega - \Omega_{bulk}}{\mathscr{A}}, \tag{4.3}$$

where Ω_{bulk} is the sum of the grand potentials of the two bulk phases and $\mathscr{A}$ is the area of the interface under consideration. It can thus be computed from the density profile. Simple analytical expressions can even be derived in the sharp-interface limit and are given in appendix B. In the case of the contact line, surface tensions for the planar wall–gas, wall–liquid and liquid–gas interfaces are obtained from the density profile constructed in figure 8. Some values for several ϵ_w are reported in table 1. A consistency check can be performed by using the isotherms of the previous section, since, for a 1D infinite system at $\mu = \mu_{sat}$,

$$\sigma_{wl} + \sigma_{lg} - \sigma_{wg} = \int_{\Gamma_0}^{+\infty} (\mu(\Gamma) - \mu_{sat})\, \mathrm{d}\Gamma, \tag{4.4}$$

where $\mu(\Gamma)$ refers to the isotherm curve and Γ_0 is the value of Γ corresponding to the microscopic film equilibrium state at $\mu = \mu_{sat}$ (which always exists in these cases). The difference between the two sides of (4.4) for the values of table 1 is at most 0.005.

From surface tension values, one can calculate the contact angle θ using Young's equation,

$$\sigma_{wg} = \sigma_{wl} + \sigma_{lg} \cos\theta, \tag{4.5}$$

and contrast it with the one obtained by a direct geometric measurement in figure 11 using density level curves. We note that the choice of the specific level curve is

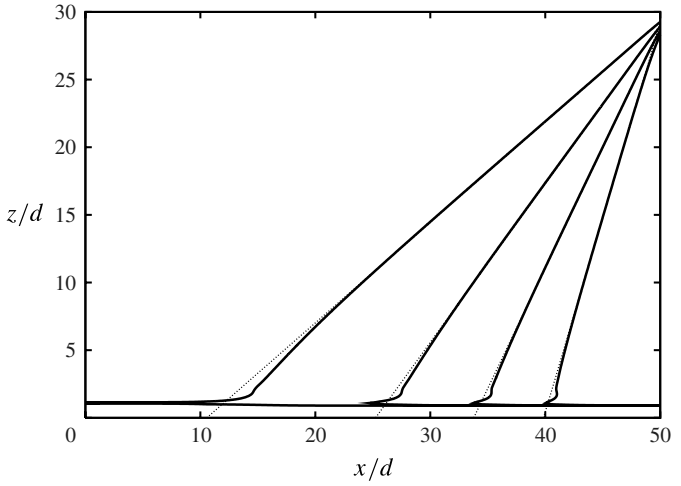

FIGURE 11. Density level curves corresponding to $(n_{liq} + n_{gas})d^3/2$ for several values of ϵ_w. From left to right: $\beta_c\epsilon_w = 1.3$, 1.2, 1.1 and 1.0. The contact angle in each case is measured by following the dotted lines. The wall potential is V_{LJ}, the temperature $T = 0.7\,T_c$ and the chemical potential $\mu = \mu_{sat}$. The wall parameters are $\sigma_w = 1.25\,d$ and $z_w = 0$.

$\beta_c\epsilon_w$	$\beta_c d^2\sigma_{wg}$	$\beta_c d^2\sigma_{wl}$	$\beta_c d^2\sigma_{lg}$	θ_{num} (°)	θ_{meas} (°)
1.0	−0.0821	−0.253	0.503	70.2	70.8
1.1	−0.106	−0.360	0.503	59.7	60.7
1.2	−0.136	−0.470	0.503	48.4	49.5
1.3	−0.171	−0.582	0.503	35.2	36.6

TABLE 1. Wall–gas (σ_{wg}), wall–liquid (σ_{wl}) and liquid–gas (σ_{lg}) surface tensions, and computed (θ_{num}) and measured (θ_{meas}) contact angles corresponding to figure 11.

not important, since, as demonstrated in figure 10, away from the contact line, the interface shape is very close to the one corresponding to the liquid–gas interface without wall, and consequently two different level curves would yield the same geometric contact angle. Results for several values of ϵ_w are given in table 1. A very good agreement is found between the two values of the contact angle. The main discrepancy between the two is quite likely caused by the error in the drawing of the dotted lines in figure 11. The computations in figure 11 also indicate that increasing the wall attraction decreases the contact angle (as expected).

Besides Young's equation, which reflects the mechanical equilibrium in a direction parallel to the wall at the contact line, there exists a relation in the normal direction, which involves the disjoining pressure (Henderson 2004),

$$\sigma_{wl}\sin\theta = -\int_{x_-}^{x_+} \Pi(x)\,\mathrm{d}x, \tag{4.6}$$

where x_- and x_+ denote the boundaries of the contact line. One can then use the isotherms computed in § 3.2 to obtain an approximate value of the contact angle from this equation. In effect, we have seen that these isotherms also represent the evolution of the adsorption Γ with respect to μ_{N_e} at a fixed temperature. In the present case

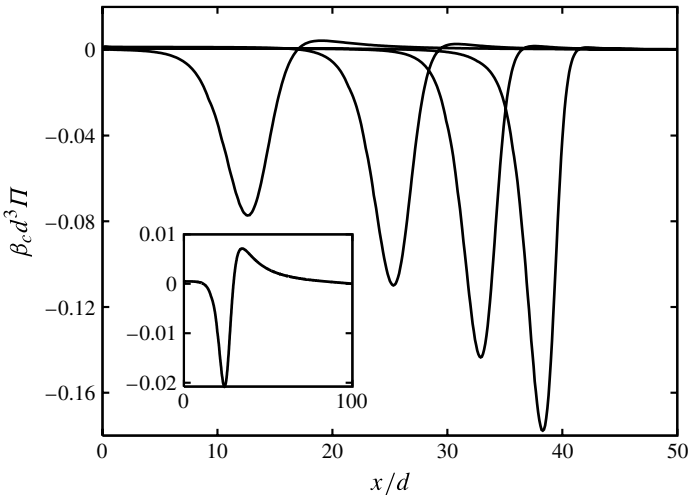

FIGURE 12. Disjoining pressure, computed by the procedure detailed in the text, as a function of the position along the substrate. From left to right: $\beta_c \epsilon_w = 1.3$, 1.2, 1.1 and 1.0, corresponding to the cases of figure 11. Inset: same plot for the case of figure 6.

(2D computations), we still have $\mu_{N_e} = \mu$ so that, as the chemical potential of the surroundings is μ_{sat}, $\mu_{N_e,0} = \mu_{sat}$. Consequently, if we denote by $\Gamma(x)$ the value of the adsorption at position x,

$$\Pi(x) \approx -(\mu(\Gamma(x)) - \mu_{sat})(n_{liq}(\mu_{sat}) - n_{gas}(\mu_{sat})),$$

where $\mu(\Gamma)$ is the value of the chemical potential that yields an adsorption equal to Γ and can be obtained from the isotherms.

The variation of the disjoining pressure as a function of the position along the substrate is depicted in figure 12. These profiles compare well with the results obtained by Herring & Henderson (2010) except that in the present case they are not symmetric. In particular, the disjoining pressure intersects the horizontal axis; this corresponds to the adsorption of the unstable solution of (3.1) for the 1D density profile at $\mu = \mu_{sat}$. The values of the contact angle obtained by applying this method are not as accurate as in the case of Young's equation. We obtain a $\sin\theta$ equal to 1.12, 1.00, 0.83 and 0.66 for $\beta_c \epsilon_w = 1.0$, 1.1, 1.2 and 1.3, respectively. The agreement becomes better as the contact angle decreases, i.e. as the slope of the film thickness as well as the departure from zero of the disjoining pressure get smaller. By contrast, the same procedure applied to the case of § 4.2 yields for the integral of the disjoining pressure (depicted in the inset in figure 12) a value smaller than 10^{-3}: as we have two equilibrium film profiles on each side of the transition area, the total force in the normal direction is zero.

4.4. *Contact line*

A close inspection of the contact line area in figure 11 reveals a deviation between the geometric profile suggested by Young's equation and the one obtained from DFT close to the contact line where the interface seems to bend towards the wall and away from the dotted lines corresponding to Young's equation. This feature appears to be in agreement with recent experiments by Seemann *et al.* (2005). The experiments were actually done for a two-layer composite wall, but when the top layer is thin, the interface close to the contact line appears to be similar to that shown in figure 11.

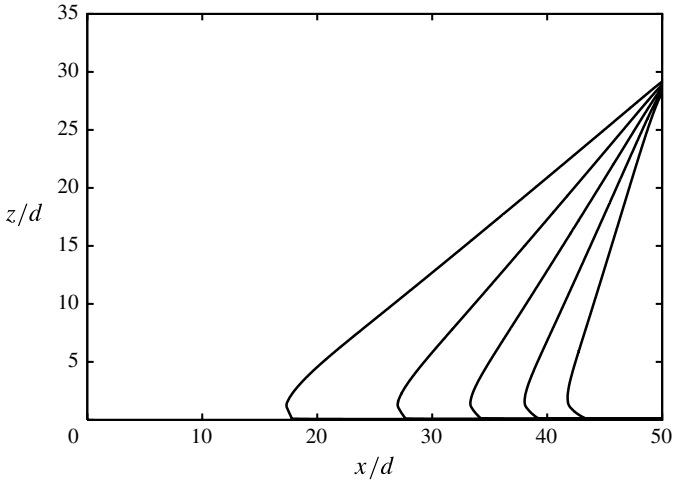

FIGURE 13. Density level curves corresponding to $(n_{liq} + n_{gas})d^3/2$ for wall potential V_{SR} and several values of ϵ_w. From left to right: $\beta_c\epsilon_w = 1.8$, 1.7, 1.6, 1.5 and 1.4. The temperature is $T = 0.7\,T_c$ and the chemical potential $\mu = \mu_{sat}$, while the wall parameters are $\sigma_w = 1.25\,d$ and $z_w = 0$.

Level curves constructed with wall potentials V_{SR} and V_{LR} in (2.4*a*) and (2.4*b*) are given in figures 13 and 14, respectively. The bend is not present in the first case, which suggests that it is mainly due to the long-range nature of the attraction of the wall potential. A parallel can be made with the conclusions of § 4.2 regarding the density shape in the transition area between the two films: as the contact angle goes to zero, the profiles in figure 13 seem to tend to the one in figure 7, giving rise to an abrupt transition between the two films, while the ones in figure 14 seem to lead to the profile in figure 6, for which a smoother transition between the two films is observed. In contrast, no dramatic difference is observed between V_{LJ} (figure 11) and V_{LR} (figure 14), implying that the shape of the repulsive part of the wall potential is less critical.

Cuts in the contact line area normal to the wall are shown in figure 15 for the two potentials V_{SR} and V_{LR} in (2.4*a*) and (2.4*b*), respectively. We note that the density profiles are characterized by a small depression in the immediate vicinity of the wall ($x/d \approx 0.5$), although this feature disappears in the case of the short-range wall potential V_{SR} as we move away from the contact line towards the liquid.

5. Summary

We have examined the equilibrium of a fluid in contact with a solid substrate through a DFT theory based on a perturbation approach in which the interaction potential is split into a repulsive and an attractive part. This leads to three distinct parts in the expression for the free-energy functional, corresponding to repulsion, attraction and external potential associated with the presence of the solid boundary, respectively.

For the 1D case of a liquid film in contact with the substrate and for values of the chemical potential less than but close to its saturation value, a liquid film exists in contact with the wall, even though, in the absence of the wall, the gas is the preferred state. The presence of the film is due to the attractive part of the wall potential. For a

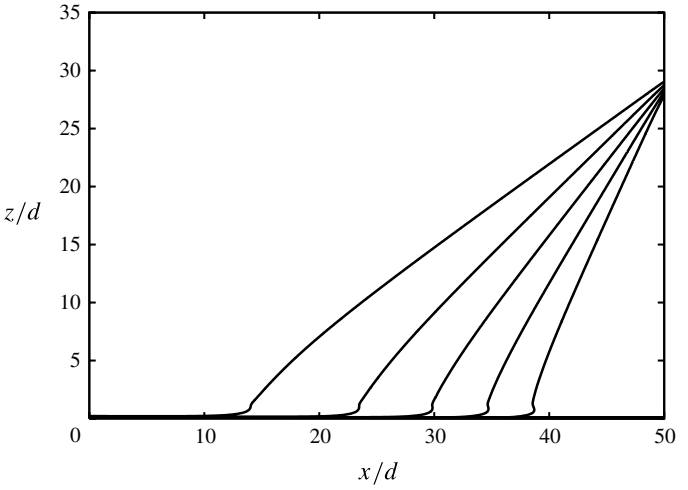

FIGURE 14. Density level curves corresponding to $(n_{liq} + n_{gas})d^3/2$ for wall potential V_{LR} and several values of ϵ_w. From left to right: $\beta_c\epsilon_w = 2.1$, 2.0, 1.9, 1.8 and 1.7. The temperature is $T = 0.7\,T_c$ and the chemical potential $\mu = \mu_{sat}$, while the wall parameters are $\sigma_w = 1.25\,d$ and $z_w = 0$.

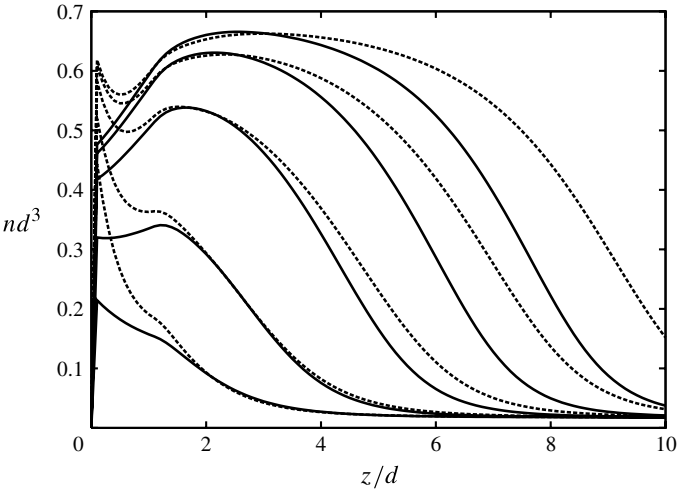

FIGURE 15. Density profiles around the contact line area for the cases depicted in figure 13 ($\beta_c\epsilon_w = 1.8$, solid lines) and in figure 14 ($\beta_c\epsilon_w = 2.0$, dotted lines). Bottom/top curves correspond to the left/right of the contact line region in steps of 2 for x/d.

given temperature, we have constructed bifurcation diagrams for the film thickness as a function of the chemical potential. Such diagrams are typically S-shaped curves with three branches. Comparison of the DFT theory with a gradient approach in which the integral DFT equation is approximated with a differential one reveals some significant qualitative differences. Any gradient approach is by definition a local one and as such

it neglects the non-local features induced by the intermolecular forces acting on the fluid system.

The bifurcation diagrams reveal that there exists a special value of the chemical potential, which we referred to as 'coexistence' value, in which a thin liquid film is equally stable with a thick one ('prewetting transition'). The interface that joins the two films is constructed with a fully 2D computation, as now the translational invariance of the system in the direction parallel to the wall is broken. As the coexistence value tends to the saturation one, the thickness of the thick film tends to infinity. This then allows us to construct a liquid wedge in contact with the substrate and with a well-defined three-phase contact line. This wedge seems to persist for all distances from the substrate and hence it should eventually enter the macroscale. Comparison of the geometric contact angle with the one obtained from the DFT theory through the transverse and normal components of Young's force balance shows good agreement and allows for the investigation of the contact line region from well-defined intermolecular parameters only.

Of particular interest would be the extension of this approach to: (i) spatially heterogeneous, chemical or topographical substrates – such substrates have a significant effect on the wetting characteristics of the solid–liquid pair (e.g. Schwartz & Eley 1998; Gramlich, Mazouchi & Homsy 2004; Quéré 2007; Savva & Kalliadasis 2009; Savva, Kalliadasis & Pavliotis 2010); and (ii) the substantially more involved dynamic case – this would form the basis for the formulation of a dynamic contact angle theory from first principles without the need for any phenomenological parameters. We shall examine these problems in future studies.

Acknowledgements

We are grateful to the anonymous referees for helpful comments and suggestions, and to A. Malijevský, A. Nold and P. Yatsyshin for stimulating discussions. We are also grateful to N. Savva for assistance, critical reading of the manuscript and stimulating discussions. We acknowledge financial support from EPSRC Platform Grant No. EP/E046029 and ERC Advanced Grant No. 247031.

Appendix A. Fluid modelling

Several approximations for $F[n]$ have been proposed over the years. One that has proved to be successful in a number of cases is based on a perturbation approach (Evans 1979; Plischke & Bergersen 2006). The basic idea is to split the pair potential $\phi(r_{12})$ into two terms: $\phi(r_{12}) = \phi_r(r_{12}) + \phi_p(r_{12})$. The first term, $\phi_r(r_{12})$, is a reference potential and usually corresponds to the harshly repulsive part of $\phi(r_{12})$; while the second term, $\phi_p(r_{12})$, acts as a 'perturbation' to $\phi_r(r_{12})$ and is in general a slowly attractive potential. Such separation is in general well suited for treating dense fluids. Its underlying physical motivation is that the structure of a fluid is determined mainly by the repulsive forces. After some additional simplifications, we have the following compact expression for $F[n]$ (Evans 1979; Plischke & Bergersen 2006):

$$F[n] = F_r[n] + \frac{1}{2}\iint \mathrm{d}\boldsymbol{r}\,\mathrm{d}\boldsymbol{r}'\; n(\boldsymbol{r})n(\boldsymbol{r}')\phi_p(|\boldsymbol{r}-\boldsymbol{r}'|). \tag{A 1a}$$

The first term of (A 1*a*) accounts for $\phi_r(r_{12})$ and can be further simplified by using the so-called local density approximation:

$$F_r[n] = \int \mathrm{d}\boldsymbol{r}\, n(\boldsymbol{r}) f(n(\boldsymbol{r})), \tag{A 1b}$$

where f is the local free energy per particle of the reference fluid. The second term of (A 1*a*), in which the pairwise distribution function is approximated by just the product of $n(\boldsymbol{r}_1)$ and $n(\boldsymbol{r}_2)$, involves the attractive part of the interaction potential $\phi(r_{12})$ (see equation (52) in Evans 1979). Expressions such as (A 1*a*) and (A 1*b*) for the free energy of a fluid date back to van der Waals, who first proposed an expression involving the local free energy plus a gradient term.

The decomposition of the pair potential into two parts can be done in different ways. In the Barker–Henderson approach, for example, (Barker & Henderson 1967), the attractive part is

$$\phi_p(r_{12}) = \begin{cases} 0 & \text{if } r_{12} < \sigma, \\ 4\epsilon \left[\left(\dfrac{\sigma}{r_{12}} \right)^{12} - \left(\dfrac{\sigma}{r_{12}} \right)^{6} \right] & \text{if } r_{12} > \sigma, \end{cases} \tag{A 2}$$

where ϵ is a parameter that measures the strength of the potential. Another possibility is the decomposition suggested by Weeks, Chandler & Andersen (1971). Here we adopt the Barker–Henderson approach. The reference potential is then $\phi_r = \phi - \phi_p$. However, to take full advantage of the perturbation technique, the reference system should be a well-known fluid. The preferred choice is often a hard-sphere fluid, whose bulk local free energy is well described by the Carnahan–Starling expression:

$$\beta f(T, n) = \ln(\Lambda^3 n) - 1 + \frac{\eta(4 - 3\eta)}{(1 - \eta)^2}, \tag{A 3a}$$

where

$$\eta \equiv \frac{\pi}{6} d^3 n \tag{A 3b}$$

is the packing fraction, d is the hard-sphere diameter, Λ is the thermal de Broglie length and $\beta \equiv 1/(k_B T)$, with k_B the Boltzmann constant. This means that ϕ_r is in fact approximated by a hard-sphere potential. The associated molecular diameter d, which appears in (A 3*b*) and hence (A 3*a*), can be linked to σ and the reference part of the interaction potential (Barker & Henderson 1967) but for simplicity we assume $d = \sigma$. Note that Λ is actually never used, as it appears in an additive constant in the expression of β times the chemical potential of the reference system (see below).

Instead of (A 1*b*) and (A 3*a*), one could use a more refined approach for a hard-sphere fluid based on Rosenfeld's fundamental measure theory (Rosenfeld 1989). In general, this approach gives better results for the fluid density at small distances from the substrate (a few molecular diameters) but requires a more involved computational treatment. Another deficiency of the model concerns the treatment of fluctuations, in particular the interfacial ones. A more detailed account on this issue is given in Evans (1979) and Henderson (2005). Our aim here is to keep the formalism as simple as possible and yet retain the basic ingredients of the underlying physics.

By substituting (A 1*a*) and (A 1*b*) into (2.3), we obtain, for $\boldsymbol{r} \in \mathscr{D}$,

$$\mu_r(n(\boldsymbol{r})) + \int \mathrm{d}\boldsymbol{r}'\, n(\boldsymbol{r}') \phi_p(|\boldsymbol{r} - \boldsymbol{r}'|) + V_{ext}(\boldsymbol{r}) = \mu, \tag{A 4a}$$

where

$$\mu_r(n) \equiv \left(\frac{\partial (nf(T,n))}{\partial n} \right)_T \tag{A 4b}$$

is the chemical potential of the reference system, which in the case of a hard-sphere fluid and using (A 3*a*) reads

$$\beta \mu_r(n) = \ln(\Lambda^3 n) + \frac{\eta(8 - 9\eta + 3\eta^2)}{(1-\eta)^3}. \tag{A 5}$$

When the wall potential vanishes and the fluid density is uniform, i.e. it does not exhibit any spatial variation, (A 1*a*) combined with (A 1*b*) reduces to

$$F[n] = \mathscr{V} n \bar{f}(n) + o(\mathscr{V}), \tag{A 6a}$$

where

$$\bar{f}(n) = f(n) - \alpha n \quad \text{and} \quad \alpha = -\frac{1}{2} \iiint_{-\infty}^{+\infty} \mathrm{d}\boldsymbol{r}\, \phi_p(|\boldsymbol{r}|). \tag{A 6b}$$

Note that the integral in the definition of α converges and the function $\bar{f}$ does not depend on external conditions (except T). Equation (A 4) is then an algebraic equation with parameters T and μ. Using for f the expression given in (A 3*a*), the usual thermodynamics for liquid–gas systems applies. The solutions to (A 4) correspond to extrema of the functional $\Omega[n]$. There is one solution for $T > T_c$ and one to three solutions for $T < T_c$, where T_c is the critical temperature ($\beta_c \equiv 1/(k_B T_c)$). In the latter case, there are two minima of equal depth for Ω, at small and large densities, respectively, and a maximum at intermediate densities. The middle solution is unstable while the other two correspond to the liquid and gas bulk densities, denoted as $n_{gas}(T,\mu)$ and $n_{liq}(T,\mu)$, respectively, with $n_{gas}(T,\mu) < n_{liq}(T,\mu)$. The chemical potential at the gas–liquid transition will be denoted as $\mu_{sat}(T)$. The gas is the preferred state for $\mu < \mu_{sat}(T)$. At $\mu = \mu_{sat}(T)$ the gas and liquid bulk are at equilibrium, while for $\mu > \mu_{sat}(T)$ the liquid is the preferred state. Note that in all cases considered here $T < T_c$.

Appendix B. Expressions

B.1. *Surface tensions*

For a planar interface (i.e. the 1D case), analytical expressions for the surface tensions can be derived in the sharp-interface limit for an infinite system. They read

$$\sigma_{lg} = -\tfrac{1}{2} (n_{liq} - n_{gas})^2 I, \tag{B 1a}$$

$$\sigma_{wg} = -\tfrac{1}{2} n_{gas}^2 I + n_{gas} \int_0^{+\infty} \mathrm{d}z\, V(z), \tag{B 1b}$$

$$\sigma_{wl} = -\tfrac{1}{2} n_{liq}^2 I + n_{liq} \int_0^{+\infty} \mathrm{d}z\, V(z), \tag{B 1c}$$

where

$$I = \int_{-\infty}^{0} \mathrm{d}z \int_0^{+\infty} \mathrm{d}z'\, \Phi_{1d}(z' - z). \tag{B 1d}$$

Such expressions are also applicable in the contact angle case sufficiently far from the contact line, i.e. when the interface is planar.

B.2. *Interaction potential*

In this subsection, we provide analytical expressions for Φ used in the 1D and 2D computations. This quantity is defined from the perturbative part of the interaction potential between fluid molecules, which in the Barker–Henderson model reads

$$\phi_p(r) = \begin{cases} 0 & \text{if } r < \sigma, \\ 4\epsilon \left[\left(\dfrac{\sigma}{r}\right)^{12} - \left(\dfrac{\sigma}{r}\right)^{6} \right] & \text{if } r > \sigma. \end{cases} \tag{B 2}$$

In the 1D case, Φ, which enters the equation for the density, is defined as

$$\Phi_{1d}(Z) = \iint_{-\infty}^{+\infty} \mathrm{d}x\,\mathrm{d}y\,\phi_p\left(\sqrt{x^2+y^2+Z^2}\right). \tag{B 3}$$

Let us introduce $\bar{Z} = Z/\sigma$. Using (B 2), we obtain

$$\Phi_{1d} = \begin{cases} -2\pi\epsilon\sigma^2 \dfrac{3}{5} & \text{if } |\bar{Z}| \leqslant 1, \\ 2\pi\epsilon\sigma^2 \dfrac{1}{\bar{Z}^4}\left(\dfrac{2}{5}\dfrac{1}{\bar{Z}^6} - 1\right) & \text{if } |\bar{Z}| > 1. \end{cases} \tag{B 4}$$

In the 2D case Φ is defined as

$$\Phi_{2d}(R) = \int_{-\infty}^{+\infty} \mathrm{d}y\,\phi_p\left(\sqrt{y^2+R^2}\right). \tag{B 5}$$

Let us define $\bar{R} = R/\sigma$. For $\bar{R} < 1$ we obtain

$$\begin{aligned} \Phi_{2d} = 8\epsilon\sigma \Bigg\{ & \frac{1}{\bar{R}^{11}} \left[\frac{63}{256} \arcsin(\bar{R}) \right. \\ & \left. - \sqrt{1-\bar{R}^2} \frac{\bar{R}(128\bar{R}^8 + 144\bar{R}^6 + 168\bar{R}^4 + 210\bar{R}^2 + 315)}{1280} \right] \\ & - \frac{1}{\bar{R}^5} \left[\frac{3}{8} \arcsin(\bar{R}) - \sqrt{1-\bar{R}^2} \frac{\bar{R}(2\bar{R}^2+3)}{8} \right] \Bigg\}, \end{aligned} \tag{B 6}$$

(note that the limit of Φ_{2d} as $\bar{R} \to 0$ exists), and for $\bar{R} \geqslant 1$ we have

$$\Phi_{2d} = \frac{3}{2}\epsilon\pi\sigma \frac{1}{\bar{R}^5} \left[\frac{21}{32} \frac{1}{\bar{R}^6} - 1 \right]. \tag{B 7}$$

Appendix C. Numerical methods

C.1. *1D case*

The equation to solve reads

$$\mu_r[n](z) + \int_{-\infty}^{+\infty} \mathrm{d}z'\, n(z') \Phi_{1d}(z'-z) + V(z) = \mu, \tag{C 1}$$

for $n(z)$ in the domain $\mathscr{D}_{1d} =]z_0, z_{N_z}[$, with conditions $n = n_b$ for $z \leqslant z_0$ and $n = n_t$ for $z \geqslant z_{N_z}$. In the presence of the wall, we assume $z_0 \geqslant z_w$. We introduce a uniform mesh: $z_i = z_0 + \Delta z\, i$, $i = 0, \ldots, N_z$. The integral is computed by using a trapezoidal rule

in the interval $[z_0, z_{N_z}]$, while analytical expressions are utilized outside this interval, obtained by using (B 4) and the fact that the density there is constant ($n = n_b$ or $n = n_t$). We then obtain a system of $N_z - 1$ nonlinear equations for the unknowns $n_i = n(z_i)$, $i = 1, \ldots, N_z - 1$, which are solved by using a Newton scheme. In order to speed up the scheme, the off-diagonal elements of the Jacobian matrix are neglected, as they are smaller compared to the diagonal ones (this is especially so far from the diagonal). The Jacobian matrix can then be inverted analytically in each iteration step.

C.2. *2D case*

The equation to solve reads

$$\mu_r[n](x,z) + \iint_{-\infty}^{+\infty} \mathrm{d}x'\,\mathrm{d}z'\, n(x',z')\Phi_{2d}\left(\sqrt{(x'-x)^2+(z'-z)^2}\right) + V(x,z) = \mu, \quad \text{(C 2)}$$

for $(x,z) \in \mathscr{D}_{2d}$, where $\mathscr{D}_{2d} =]x_0, x_{N_x}[\times]z_0, z_{N_z}[$. In the presence of a wall, $z_0 \geqslant z_w$. The conditions outside this domain are $n(x,z) = n_l(z)$ if $x \leqslant x_0$, $n(x,z) = n_r(z)$ if $x \geqslant x_{N_x}$, $n(x,z) = n_b$ if $z \leqslant z_0$, and $n(x,z) = n_t$ if $z \geqslant z_{N_z}$. The functions n_l and n_r are such that $n_l(z) = n_b$ and $n_r(z) = n_b$ if $z \leqslant z_0$, and $n_l(z) = n_t$ and $n_r(z) = n_t$ if $z \geqslant z_{N_z}$. This choice of conditions for $x \leqslant x_0$ and $x \geqslant x_{N_x}$ allows us to examine, for example, the case of a fluid in contact with two liquid films of different thicknesses, one on each side.

A uniform mesh is used to compute $n(x,z)$: $x_j = x_0 + \Delta x j$, $j = 0, \ldots, N_x$, and $z_i = z_0 + \Delta z\, i$, $i = 0, \ldots, N_z$. Equation (C 2) is solved for $n_{ji} = n(x_j, z_i)$, $j = 1, \ldots, N_x - 1$ and $i = 1, \ldots, N_z - 1$. The integral appearing in the equation is computed by dividing the integration domain into three parts: $\mathscr{D}_{2d}$, $\mathscr{D}'_{2d} - \mathscr{D}_{2d}$ and $]-\infty, +\infty[\times]-\infty, +\infty[- \mathscr{D}'_{2d}$. The domain $\mathscr{D}'_{2d}$ is defined as $\mathscr{D}'_{2d} =]x'_0, x'_{N_x}[\times]z'_0, z'_{N_z}[$, where $x'_0 = x_0 - \sigma$, $x'_{N_x} = x_{N_x} + \sigma$, $z'_0 = z_0 - \sigma$ and $z'_{N_z} = z_{N_z} + \sigma$. Outside $\mathscr{D}'_{2d}$, (B 7) is used for any $n_{ji} \in \mathscr{D}_{2d}$ and analytical expressions can be derived for the integral when $|x', z'| \to \infty$ where the density is constant ($n = n_b$ or $n = n_t$). In $\mathscr{D}'_{2d} - \mathscr{D}_{2d}$, the integral is computed numerically by using either (B 6) or (B 7) once for all at the start of a run. In $\mathscr{D}_{2d}$, the integral has to be carried out numerically at each iteration.

The discretization of (C 2) leads to a set of $(N_x - 1) \times (N_z - 1)$ nonlinear equations for the $(N_x - 1) \times (N_z - 1)$ unknowns n_{ji}. It is solved by using a Newton scheme. To speed up the computations, the Jacobian is made sparse by neglecting contributions when $|\boldsymbol{r}_1 - \boldsymbol{r}_2|$, where $\boldsymbol{r}_{1,2}$ are the positions of two particles, is larger than a few molecular diameters. Indeed, since the non-diagonal terms of the Jacobian involve $\Phi_{2d}(\boldsymbol{r}_1 - \boldsymbol{r}_2)$ (for the diagonal terms $\boldsymbol{r}_1 - \boldsymbol{r}_2 = 0$), they become small as we move further from the diagonal (as $|\boldsymbol{r}_1 - \boldsymbol{r}_2|$ increases, Φ_{2d} decreases). By doing so, more iterations are needed for convergence but each one is considerably faster than inverting the full Jacobian. Finally, at each iteration step, we have to solve a linear system involving a sparse matrix. This stage is performed with a Gauss–Siedel method.

Appendix D. Square gradient approach

A substantial simplification to (A 1*a*) can be achieved if we assume that $n(\boldsymbol{r})$ varies smoothly in the range of ϕ_p. Indeed, by expanding $n(\boldsymbol{r})$ in a Taylor series and neglecting terms of $O(3)$ and higher, (A 1*a*) becomes

$$F[n] = F_r[n] + \int \mathrm{d}\boldsymbol{r}\left(\frac{K}{2}\,|\nabla n(\boldsymbol{r})|^2 - \alpha n^2(\boldsymbol{r})\right), \quad \text{(D 1a)}$$

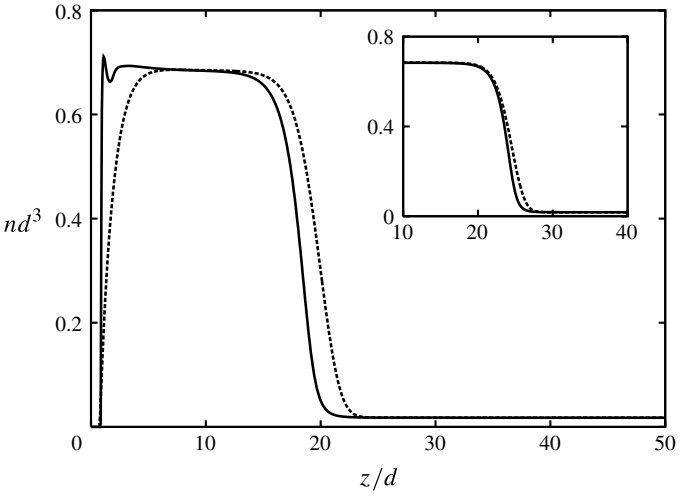

FIGURE 16. Density profiles obtained by solving (A 4) (solid line) and (D 2) (dotted line) in the presence of a wall for $T = 0.7\,T_c$ and $\mu - \mu_{sat}(T) = -0.001 k_B T_c$. The wall potential is V_{LJ} with parameters $\beta_c \epsilon_w = 1.8$, $\sigma_w = 1.25\,d$ and $z_w = 0$. Inset: Density profiles obtained by solving (A 4) (solid line) and (D 2) (dotted line) for $T = 0.7\,T_c$ and $\mu = \mu_{sat}(T)$.

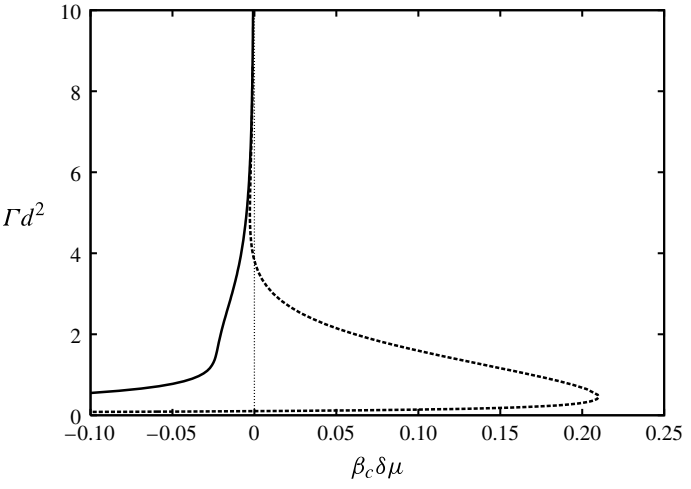

FIGURE 17. Isotherms obtained by solving (A 4) (solid line) and (D 2) (dotted line) for $T = 0.8\,T_c$. The wall potential is V_{LJ} with parameters $\beta_c \epsilon_w = 1.4$, $\sigma_w = 1.25\,d$ and $z_w = 0$. The dividing interface is located at $z_I = z_w$.

where

$$K = -\frac{2\pi}{3} \int \mathrm{d}r\, r^4 \phi_p(r). \tag{D 1b}$$

Instead of the integral equation (A 4), where $F_r[n]$ is given by (A 1*b*), we now have a differential equation

$$\mu_r(n) - K\Delta n - 2\alpha n + V(\boldsymbol{r}) = \mu. \tag{D 2}$$

This local approach has been widely used to compute 1D density profiles (e.g. Teletzke, Scriven & Davis 1982). It is also the starting point of Cahn–Hilliard type/diffuse interface equations where the free energy is typically a function of density and its gradient (e.g. Miranville 2003). However, comparison with the DFT integral approach reveals a number of shortcomings, especially when it comes to interfaces. The inset of figure 16 shows the liquid–gas interface obtained by solving (A 4) and (D 2). Although the overall shape of the density profile is qualitatively similar for the two cases, differences appear in the transition area, where $n(\boldsymbol{r})$ varies sharply. This is even more evident when a wall is present, as demonstrated in figure 16. The local approach leads to smoother curves with milder slopes and is unable to account for the small oscillations near the wall.

Qualitative differences can appear between the two methods when considering the isotherms. For example, in figure 17 the local approach shows a multi-valued curve, and hence phase transition, as opposed to a single-valued curve obtained from the integral approach.

Differences between local and non-local approaches have also been examined in previous studies, for example by Getta & Dietrich (1998, and references therein) in the context of contact lines. However, in contrast with the present study, they used a so-called effective interface potential for which a sharp-interface approximation is made in the direction normal to the substrate.

REFERENCES

ARGAMAN, N. & MAKOV, G. 2000 Density functional theory: An introduction. *Am. J. Phys.* **68**, 69–79.

BARKER, J. A. & HENDERSON, D. 1967 Perturbation theory and equation of state for fluids. II. A successful theory of liquids. *J. Chem. Phys.* **47**, 4714.

BAUER, C. & DIETRICH, S. 1999 Quantitative study of laterally inhomogeneous wetting films. *Eur. Phys. J. B* **10**, 767.

BERIM, G. O. & RUCKENSTEIN, E. 2008*a* Microscopic calculation of the sticking force for nanodrops on an inclined surface. *J. Chem. Phys.* **129**, 114709.

BERIM, G. O. & RUCKENSTEIN, E. 2008*b* Nanodrop on a nanorough solid surface: density functional theory considerations. *J. Chem. Phys.* **129**, 014798.

BERIM, G. O. & RUCKENSTEIN, E. 2009 Simple expression for the dependence of the nanodrop contact angle on liquid–solid interactions and temperature. *J. Chem. Phys.* **130**, 044709.

BONN, D., EGGERS, J., INDEKEU, J., MEUNIER, J. & ROLLEY, E. 2009 Wetting and spreading. *Rev. Mod. Phys.* **81**, 739.

DUSSAN, E. B. V & DAVIS, S. H. 1974 On the motion of a fluid–fluid interface along a solid surface. *J. Fluid Mech.* **65**, 71–95.

EVANS, R. 1979 The nature of the liquid–vapour interface and other topics in the statistical mechanics of non-uniform, classical fluids. *Adv. Phys.* **28**, 143.

EVANS, R. 1992 Density functionals on the theory of non-uniform fluids. In *Fundamentals of Inhomogeneous Fluids* (ed. D. Henderson), pp. 85–176. Marcel Dekker.

EVANS, R. & PARRY, A. 1990 Liquids at interfaces: what can a theorist contribute? *J. Phys.: Condens. Matter* **2**, SA15–SA32.

DE GENNES, P.-G. 1985 Wetting: Statics and dynamics. *Rev. Mod. Phys.* **57**, 827.

GETTA, T. & DIETRICH, S. 1998 Line tension between fluid phases and a substrate. *Phys. Rev.* E **57**, 655.

GRAMLICH, C. M., MAZOUCHI, A. & HOMSY, G. M. 2004 Time-dependent free surface Stokes flow with a moving contact line. II. Flow over wedges and trenches. *Phys. Fluids* **16**, 1660–1667.

HENDERSON, J. R. 2004 Statistical mechanics of fluids adsorbed in planar wedges: Finite contact angle. *Phys. Rev.* E **69**, 061613.

HENDERSON, J. R. 2005 Statistical mechanics of the disjoining pressure of a planar film. *Phys. Rev.* E **72**, 051602.

HERRING, A. R. & HENDERSON, J. R. 2010 Simulation study of the disjoining pressure profile through a three-phase contact line. *J. Chem. Phys.* **132**, 084702.

HUH, C. & SCRIVEN, L. E. 1971 Hydrodynamic model of steady movement of a solid/liquid/fluid contact line. *J. Colloid Interface Sci.* **35**, 85–101.

INDEKEU, J. O. 1994 Line tension at wetting. *Intl J. Mod. Phys.* B **8**, 309.

LANDAU, L. D. & LIFSHITZ, E. M. 1980 *Statistical Physics,* Part I. Pergamon.

MIRANVILLE, A. 2003 Generalized Cahn–Hilliard equations based on a microforce balance. *J. Appl. Maths* **4**, 165–185.

MOFFAT, H. K. 1963 Viscous and resistive eddies near a sharp corner. *J. Fluid Mech.* **18**, 1–18.

NOLD, A., MALIJEVSKÝ, A. & KALLIADASIS, S. 2011*a* Critical assessment of effective interfacial potentials based on a density functional theory for wetting phenomena on curved substrates. *Eur. Phys. J. Special Topics* **197**, 185–191.

NOLD, A., MALIJEVSKÝ, A. & KALLIADASIS, S. 2011*b* Wetting on a spherical wall: Influence of liquid–gas interfacial properties. *Phys. Rev.* E **84**, 021603.

PISMEN, L. M. 2002 Mesoscopic hydrodynamics of contact line motion. *Colloids Surf.* A **206**, 11.

PLISCHKE, M. & BERGERSEN, B. 2006 *Equilibrium Statistical Physics*. World Scientific.

QUÉRÉ, D. 2007 Three-phase capillarity. In *Thin Films of Soft Matter* (ed. S. Kalliadasis & U. Thiele). pp. 115–136. Springer.

ROSENFELD, Y. 1989 Free-energy model for the inhomogeneous hard-sphere fluid mixture and density-functional theory of freezing. *Phys. Rev. Lett.* **63**, 980.

SAVVA, N. & KALLIADASIS, S. 2009 Two-dimensional droplet spreading over topographical substrates. *Phys. Fluids* **21**, 092102.

SAVVA, N., KALLIADASIS, S. & PAVLIOTIS, G. A. 2010 Two-dimensional droplet spreading over random topographical substrates. *Phys. Rev. Lett.* **104**, 084501.

SCHICK, M. 1990 Introduction to wetting phenomena. In *Liquids at Interfaces, Les Houches, Session XLVIII* (ed. J. Chavrolin, J. F. Joanny & J. Zinn-Justin). p. 415. Elsevier.

SCHWARTZ, L. W. & ELEY, R. R. 1998 Simulation of droplet motion on low-energy and heterogeneous surfaces. *J. Colloid Interface Sci.* **202**, 173–188.

SEEMANN, R., HERMINGHAUS, S., NETO, C., SCHLAGOWSKI, S., PODZIMEK, D., KONRAD, R., MANTZ, H. & JACOBS, K. 2005 Dynamics and structure formation in thin polymer melt films. *J. Phys. Condens. Matter* **17**, S267–S290.

SULLIVAN, D. E. 1981 Surface tension and contact angle of a liquid–solid interface. *J. Chem. Phys.* **74**, 2604–2615.

TARAZONA, P. 1985 Free-energy density functional for hard spheres. *Phys. Rev.* A **31**, 2672–2679.

TARAZONA, P. & EVANS, R. 1983 Wetting transitions at models of a solid–gas interface. *Mol. Phys.* **48**, 799–831.

TARAZONA, P., DA GAMA, M. M. T. & EVANS, R. 1983 Wetting transitions at fluid–fluid interfaces. I. The order of the transition. *Mol. Phys.* **49**, 283–300.

TELETZKE, G. F., SCRIVEN, L. E. & DAVIS, H. T. 1982 Gradient theory of wetting transitions. *J. Colloid Interface Sci.* **87**, 550–571.

WEEKS, J. D., CHANDLER, D. & ANDERSEN, H. C. 1971 Role of repulsive forces in determining the equilibrium structure of simple liquids. *J. Chem. Phys.* **54**, 5237.